

## Coking-Resistant Iron Catalyst in Ethane Dehydrogenation Achieved through Siliceous Zeolite Modulation

Zhiyuan Yang,<sup>||</sup> Huan Li,<sup>||</sup> Hang Zhou,<sup>||</sup> Liang Wang,\* Lingxiang Wang, Qiuyan Zhu, Jianping Xiao,\* Xiangju Meng, Junxiang Chen, and Feng-Shou Xiao\*Cite This: *J. Am. Chem. Soc.* 2020, 142, 16429–16436

Read Online

ACCESS |



Metrics &amp; More

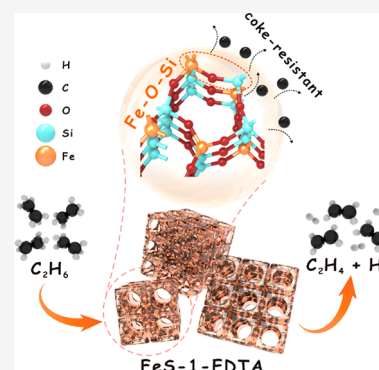


Article Recommendations



Supporting Information

**ABSTRACT:** Nonoxidative dehydrogenation is promising for production of light olefins from shale gas, but current technology relies on precious Pt or toxic Cr catalysts and suffers from thermodynamically oriented coke formation. To solve these issues, the earth-abundant iron catalyst is employed, where Fe species are effectively modulated by siliceous zeolite, which is realized by the synthesis of Fe-containing MFI siliceous zeolite in the presence of ethylenediaminetetraacetic sodium (FeS-1-EDTA). Catalytic tests in ethane dehydrogenation show that this catalyst has a superior coke resistance in a 200 h run without any deactivation with extremely high activity and selectivity (e.g., 26.3% conversion and over 97.5% selectivity to ethene in at 873 K, close to the thermodynamic equilibrium limitation). Multiple characterizations demonstrate that the catalyst has uniformly and stably isolated Fe sites, which improves ethane dehydrogenation to facilitate the fast desorption of hydrogen and olefin products in the zeolite micropores and hinders the coke formation, as also identified by density functional calculations.



## ■ INTRODUCTION

Light olefins such as ethene and propene, which are well known as raw chemicals of the modern chemical industry, have been widely used for the production of fibers, plastics, electronic devices, and higher olefins from controllable polymerization.<sup>1–6</sup> The current route for production of the light olefins is via the stream cracking of large hydrocarbons from naphtha in crucial oil or the coupling of C<sub>1</sub> molecules.<sup>5,6</sup> The alternative route is to make the stream cracking of propane from shale gas to ethene. However, the aforementioned routes still have a gap between demand and supply of both propene and ethene. The direct dehydrogenation of light alkanes provides a promising route as an auxiliary to the thermal cracking for providing light olefins from shale gas,<sup>7–10</sup> but it still has problems on the insufficient efficacy.

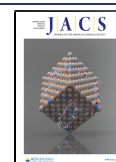
Oxidative dehydrogenation is more preferential in thermodynamics because of its exothermic feature,<sup>7,10–18</sup> while overoxidation results in invaluable CO<sub>2</sub> and CO, because the produced olefins are more reactive than the reactants (alkanes).<sup>4,14,15,19</sup> Compared with the oxidative dehydrogenation, a nonoxidative route has significant advantage in avoiding overoxidation and producing hydrogen.<sup>2,4,20–27</sup> However, the current nonoxidative dehydrogenation still suffers from poor catalyst durability, which is far to meet the demand of a process avoiding frequent catalyst regeneration. The main reason is due to catalyst deactivation, resulting from coke formation, which blocks the catalyst surface and decreases the number of accessible active sites. At the same time, the active oxide species might be reduced to lower valence under

the nonoxidative dehydrogenation conditions, eventually losing activity.<sup>4</sup> Catalyst regeneration requires shutting down the reactions, burns the coke, and regenerates the active sites. Another reason for catalyst deactivation originates from metal sintering, which reduces the active sites on the surface, as the metal nanoparticles grow to larger ones. Regeneration of the sintered catalysts requires leaching the metals and reloading them on solid carriers or a halogen treatment to redisperse the metal species, which are complex and expensive, particularly for the precious metals.

Apart from the Pt-based catalysts, the earth-abundant metals/oxides (e.g., Fe, Zn, Ga, Mo, Cr, and In) have been also used in nonoxidative dehydrogenation, but their activities and selectivities are mostly lower than those of the Pt catalysts.<sup>4,22–24,28–35</sup> Among these metals/oxides, the Fe-based catalysts are commercialized for the ethylbenzene dehydrogenation but still exhibit insufficient performance in light alkane dehydrogenation. For example, in ethane dehydrogenation, the Fe-substituted zeolite lost more than 20% of the original activity after several hours run, and the ethene selectivity was lower than 80%. The performance is even worse with the supported ferric catalysts. This phenomenon can be explained

Received: July 20, 2020

Published: August 29, 2020



by the reduction of  $\text{FeO}_x$  nanoparticles/clusters followed by carbonization to  $\text{FeC}_x$ ,<sup>36</sup> which catalyzed coke formation in the Fe–zeolites. The  $\text{FeO}_x$  aforementioned are known as extraframework oligomers at an extremely low amount. Although the Fe–zeolite catalysts have been investigated for a long time, synthesis of ideal isolated Fe is still an attractive topic.

Here, we solved these key problems and prepared ferric catalysts with both high activity and superior durability in nonoxidative dehydrogenation. With the assistance of ethylenediaminetetraacetic sodium, the isolated  $\text{Fe}^{\delta+}$  sites were successfully incorporated into the siliceous MFI zeolite framework, giving undetectable  $\text{FeO}_x$  oligomers. Such structure (named as FeS-1-EDTA) suppressed the reduction and carbonization of ferric species to maintain the active sites, facilitating the desorption of hydrogen and olefin products in the zeolite micropores. In ethane dehydrogenation, the FeS-1-EDTA exhibits a high conversion close to the thermodynamic equilibrium and ethene selectivity of  $\sim 97.5\%$ . More importantly, coke formation was effectively inhibited on the FeS-1-EDTA catalyst with stable performance in a run of 200 h.

## RESULTS AND DISCUSSION

**Synthesis and Characterization.** Fe species were incorporated into the siliceous MFI zeolite during crystallization in a hydrothermal system. First, Fe species were coordinated with ethylenediaminetetraacetic sodium (Fe–EDTA) to benefit the Fe isolation and avoid aggregation in the alkaline media. Then Fe–EDTA was added in the gel for MFI zeolite crystallization containing tetraethyl orthosilicate, tetrapropylammonium hydroxide (TPAOH), and water with a ratio of  $1.0\text{SiO}_2/0.4\text{TPAOH}/39\text{H}_2\text{O}/0.02\text{Fe}/0.02\text{EDTA}$ . After crystallization at 453 K for 4 days and calcination in air to remove the organic template and EDTA, the FeS-1-EDTA with a Fe loading at 0.8 wt % was obtained (Table S1).

Figure S1 shows XRD patterns of S-1 and FeS-1-EDTA samples, giving the peaks of the typical MFI zeolite structure.  $\text{N}_2$  sorption isothermals show the type I curves of both samples with a high surface area and pore volume (Figure S2). Scanning electron microscope (SEM) and scanning transmission electron microscope (STEM) images of the samples give direct observation of the zeolite crystals with average diameters of about 195 nm and high purity (Figures S3 and S4). These data confirm the successful synthesis of MFI zeolite.

For comparison, we also synthesized conventional Fe-substituted S-1 zeolite by direct addition of ferric precursor in the zeolite crystallization system without EDTA, denoted as FeS-1 with a Fe loading at 1.2 wt %. In addition, the Fe species were also introduced into the commercial aluminosilicate MFI zeolite by  $\text{Fe}^{2+}$  exchange and calcination, obtaining the Fe/ZSM-5-ex catalyst (Figures S5 and S6, Table S1). At the same time, the Fe species loaded on amorphous silica, ceria, and titania were synthesized from conventional impregnation with a Fe loading at 0.9–1.0 wt %, which are denoted as Fe/ $\text{SiO}_2$ , Fe/ $\text{CeO}_2$ , and Fe/ $\text{TiO}_2$ , respectively (Table S1, Figure S5).

**Ethane Dehydrogenation.** Figure 1a shows the conversion and selectivity of various catalysts in ethane dehydrogenation (EDH) at 873 K in a fixed-bed reactor under atmosphere pressure with feed gas of 30 vol %  $\text{C}_2\text{H}_6$  in Ar. The catalytic data of Fe catalysts were recorded in the steady state during continuous reaction for 2–4 h (Table S2).

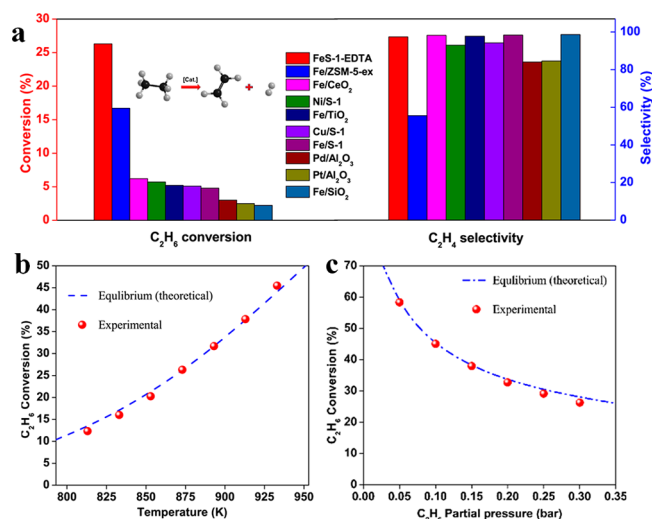


**Figure 1.** (a) Conversion and selectivity of various catalysts in EDH. Reaction conditions: 0.2 g of catalyst, 873 K, gas flowing rate at 2 L  $\text{g}_{\text{cat}}^{-1} \text{h}^{-1}$  (30% ethane balanced with Ar), and pressure at 1 atm. Dependences of ethane conversions on (b) reaction temperature and (c) feed gas concentration in the FeS-1-EDTA-catalyzed EDH. Reaction conditions are the same as those in Figure 1a, except the temperature and ethane pressure were changed. Error bounds for ethane conversion and ethene selectivity are  $\pm 2\%$  and  $\pm 0.5\%$ , respectively. Equilibrium calculations were performed through HSC Chemistry 8 software using a Gibbs free energy minimization algorithm. Side reactions (cracking and coking) were not considered in calculating the equilibrium conversions.

The possible transition metal impurities apart from Fe were excluded by inductively coupled plasma (ICP) analysis. Pure S-1 zeolite without Fe species is inactive for the reaction, giving an ethene yield  $< 1.5\%$  that is comparable to the blank run. Interestingly, the FeS-1-EDTA shows an ethane conversion of 26.3% and ethene selectivity of 97.5%, resulting in an ethene productivity of  $\sim 0.86 \text{ mol g}_{\text{Fe}}^{-1} \text{h}^{-1}$  (carbon balance higher than 99%). A slightly higher ethane conversion than the equilibrium is due to the side reactions (e.g., cracking,  $< 2.5\%$ ), which shifted the thermodynamic equilibrium and accelerated the ethane conversion (Figure S7). Under equivalent reaction conditions, the catalysts containing precious metals, such as Pt/ $\text{Al}_2\text{O}_3$  and Pd/ $\text{Al}_2\text{O}_3$  (Pd and Pt loadings of  $\sim 0.7 \text{ wt } \%$ , Figures S8–S10), exhibited poor catalytic activity with an ethane conversion of 2.5–3.1% (data recorded after 10 h reaction) and ethene selectivity at 84.1–84.7%, giving methane as the byproduct (coke was not counted in the selectivity). PtSn/ $\text{Al}_2\text{O}_3$  catalyst (Pt loading of 0.7 wt %, molar ratio of Pt/Sn = 1, Figures S11 and S12), which is a highly efficient catalyst for nonoxidative dehydrogenation, exhibited an ethane conversion of 24.1% and ethene selectivity of 85.3% (Figures S13 and S14). The methane selectivity was  $\sim 14.0\%$ , because of the cracking and coke reacting with hydrogen, which was similar to the previous observation.<sup>22</sup> In this case, the ethene productivity was  $\sim 0.39 \text{ mol g}_{\text{PtSn}}^{-1} \text{h}^{-1}$ . In contrast, FeS-1-EDTA shows better ethene selectivity and productivity than Pt-based catalysts (Figure S15), indicating its potential importance for EDH in the future.

Further evaluation was performed using the FeS-1 catalyst (Table S2), showing an ethane conversion of 7.9% and ethene productivity of  $\sim 0.18 \text{ mol g}_{\text{Fe}}^{-1} \text{h}^{-1}$ , whose performance is better than most of the Fe catalysts in EDH but still much lower than that of the FeS-1-EDTA. The Fe/ $\text{SiO}_2$ , Fe/ $\text{CeO}_2$ ,

and Fe/TiO<sub>2</sub> catalysts display relatively low ethane conversions (2.7–6.2%) and ethene productivities (0.07–0.18 mol g<sub>Fe</sub><sup>−1</sup> h<sup>−1</sup>). The S-1-supported FeO<sub>x</sub> species, which was synthesized by loading FeO<sub>x</sub> species on S-1 zeolite via impregnation [denoted as Fe/S-1], gives a low ethane conversion of 4.8% and ethene productivity of 0.16 mol g<sub>Fe</sub><sup>−1</sup> h<sup>−1</sup>. We also prepared the catalysts with similar procedures of FeS-1-EDTA for other transition metals such as Ni/S-1 and Cu/S-1 (Figures S16 and S17, Table S1), but they still show very low conversions of 5.1–5.7%. In contrast, the Fe<sup>2+</sup>-exchanged aluminosilicate zeolite (Fe/ZSM-5-ex) has higher conversion (16.7%) than the supported Fe catalyst but still obviously lower than that of FeS-1-EDTA. Ethene selectivity was only 55.6% on the Fe/ZSM-5-ex, giving a large amount of byproducts such as methane and C<sub>3+</sub> species because of the catalyst acidity.<sup>4</sup> These data confirm the exceptional performance of siliceous S-1 modulated Fe species for the EDH.

The thermodynamic equilibrium limitation and experimental ethane conversions over FeS-1-EDTA as a function of reaction temperatures and ethane partial pressures are shown in Figure 1b and 1c, respectively. The ethane conversions increase remarkably with increasing reaction temperatures or decreasing ethane partial pressures (ethane pressure was controlled by changing the ratio of Ar and ethane in the feed gas). Interestingly, the ethane conversions are always close to the theoretical limitation of the thermodynamic equilibrium, confirming the high activity of the FeS-1-EDTA catalyst.

**Durability Evaluation.** Figure 2 presents the performance of FeS-1-EDTA and Pt-based catalysts in the durability tests.

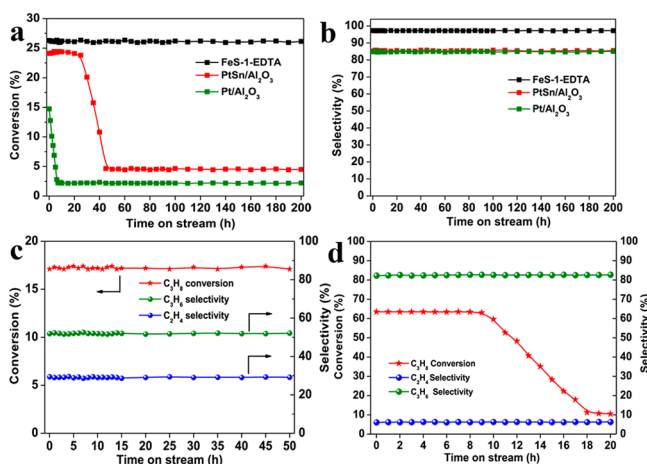


**Figure 2.** Data showing the (a) ethane conversions and (b) ethene selectivities in a long-period EDH over the FeS-1-EDTA, PtSn/Al<sub>2</sub>O<sub>3</sub>, and Pt/Al<sub>2</sub>O<sub>3</sub> catalysts. (c) Data characterizing the performance of the FeS-1-EDTA in propane dehydrogenation. (d) Data characterizing the performance of the PtSn/Al<sub>2</sub>O<sub>3</sub> in propane dehydrogenation. Reaction conditions: 0.2 g of catalyst, 873 K, gas flowing rate at 2 L g<sub>cat</sub><sup>−1</sup> h<sup>−1</sup> (30% ethane or propane balanced with Ar), pressure at 1 atm. Coke was not involved in calculating the product selectivity.

The Pt/Al<sub>2</sub>O<sub>3</sub> and PtSn/Al<sub>2</sub>O<sub>3</sub> catalysts exhibit high ethane conversions and ethene selectivities at the beginning of the reactions (Figure 2a). However, the catalytic activities are continuously decreased with the reaction time. For example, the Pt/Al<sub>2</sub>O<sub>3</sub> shows an ethane conversion of 14.8% at the beginning of 20 min and then decreases rapidly. After 6 h, the ethane conversion is as low as 2.5%. The PtSn/Al<sub>2</sub>O<sub>3</sub> shows better durability than Pt/Al<sub>2</sub>O<sub>3</sub>, in good agreement with the

known Sn promotion effect,<sup>26,29</sup> showing an ethane conversion of ~24.1% at the beginning of 30 h. However, deactivation occurs after 40 h, resulting in a final conversion of 5.0%. Thermogravimetric (TG) analysis of the deactivated catalyst demonstrates the coke formation, showing the coke weight ratios of 6.5 and 4.4 wt % on the Pt/Al<sub>2</sub>O<sub>3</sub> and PtSn/Al<sub>2</sub>O<sub>3</sub> catalysts, respectively (Figure S18). Raman spectra of the used Pt/Al<sub>2</sub>O<sub>3</sub> and PtSn/Al<sub>2</sub>O<sub>3</sub> catalysts have strong modes at 1330 and 1598 cm<sup>−1</sup>, which are assigned to the D and G bands of the carbon species (Figure S19), confirming the obvious coke formation. The fluorescent images provide direct evidence of the coke distribution on the used Pt/Al<sub>2</sub>O<sub>3</sub> and PtSn/Al<sub>2</sub>O<sub>3</sub> catalysts, exhibiting coke signals on the whole catalyst region (Figure S20).

Interestingly, the FeS-1-EDTA exhibits sustainable conversion and selectivity in the continuous reaction for 200 h, where the constant ethane conversion of ~26% is obtained. The average ethene productivity is 0.85 mol g<sub>Fe</sub><sup>−1</sup> h<sup>−1</sup> in the 200th hour, which is very close to that at the beginning of the reaction (0.86 mol g<sub>Fe</sub><sup>−1</sup> h<sup>−1</sup>). A longer reaction life can be reasonably expected because no deactivation trend is observed in the tests. After a durability test, the used FeS-1-EDTA exhibited almost unchanged activity compared with the fresh catalyst (Figure S21, data were obtained at higher mass flow to make the ethane conversion much lower than the thermodynamic equilibrium conversion and thus to persuasively evaluate the catalyst activity). These data confirm the superior durability of FeS-1-EDTA catalyst in the EDH that remarkably outperforms the supported Pt catalysts as well as the Ga- and Zn-zeolite catalysts.<sup>22</sup> TG analysis of the FeS-1-EDTA shows the coke amount to be lower than 0.7 wt % after reaction for 72 h (Figure S18). The weak Raman D/G bands (Figure S19) and fluorescence signals (Figure S20) also support the low coke amount on FeS-1-EDTA. The coke formation rate was ~0.09 mg g<sub>cat</sub><sup>−1</sup> h<sup>−1</sup> on FeS-1-EDTA, which is much lower than ~2.7 and ~1.8 mg g<sub>cat</sub><sup>−1</sup> h<sup>−1</sup> on the Pt/Al<sub>2</sub>O<sub>3</sub> and PtSn/Al<sub>2</sub>O<sub>3</sub> catalysts, respectively. Differential thermal analysis (DTA) of the used FeS-1-EDTA shows an almost undetectable exothermic signal (Figure S22). In this case, the coke might be soft oligomers that are easily removed before burning. The used FeS-1-EDTA shows similar N<sub>2</sub> sorption isotherms and surface areas to those of the fresh catalyst (Figure S23), suggesting the negligible influence of such coke to the microporosity. In contrast, DTA analysis of the used PtSn/Al<sub>2</sub>O<sub>3</sub> catalyst shows an obvious exothermic signal at 453 °C, which is in good agreement with hard coke species observed previously.<sup>37</sup> Notably, in the FeS-1-EDTA-catalyzed EDH, the methane that is usually formed in the nonoxidative EDH process has extremely low selectivity.

We further explored the catalysis of FeS-1-EDTA in the dehydrogenation of propane (Figure 2c); it also delivered constant performance with a conversion of ~17.2% and olefin selectivity of ~81.3% (ethene selectivity of 29.1%, propene selectivity of 52.2%, based on the number of carbon atoms). The activity and selectivity remain constant in the continuous reaction for 50 h. In contrast, the PtSn/Al<sub>2</sub>O<sub>3</sub> catalyst obviously loses activity in the reaction under equivalent conditions after 10 h, which is similar to the phenomenon in EDH, revealing the exceptional catalytic performance of the FeS-1-EDTA.

STEM characterization of the deactivated PtSn/Al<sub>2</sub>O<sub>3</sub> and Pt/Al<sub>2</sub>O<sub>3</sub> shows that the metal nanoparticle diameters are similar before and after catalysis (Figures S24 and S25),



confirming the coke formation dominantly leads to deactivation in the tests. Evaluation of the coking process was explored by in situ DRIFTS spectroscopy using ethene as the feed gas. As shown in Figure S26a, the in situ DRIFTS of the FeS-1-EDTA and PtSn/Al<sub>2</sub>O<sub>3</sub> show weak bands at 1481 and 1595 cm<sup>-1</sup>, assigned to the aromatic species, which is regarded as a precursor for coke formation. Prolonging the test time results in almost unchanged coke signals on the FeS-1-EDTA, confirming the coke resistance. Under equivalent conditions, the PtSn/Al<sub>2</sub>O<sub>3</sub> shows continuously enhanced coke signals (Figures S26b and S27). These data further confirm the coke resistance of the FeS-1-EDTA compared with the PtSn/Al<sub>2</sub>O<sub>3</sub> catalyst.

On the basis of the catalytic results above, the FeS-1-EDTA is an active, selective, and durable catalyst for the nonoxidative dehydration reactions, exhibiting even better performance than the Pt-based catalysts. Compared with the previous investigation on Fe–aluminosilicate zeolite, which has Fe sites with relatively low activity and acid sites that caused side reactions, the major advantage of the FeS-1-EDTA is the constant high activity with coke resistance in a long-term test.

**Structure Investigation.** Figure 3a shows UV Raman spectra of FeS-1-EDTA during different reaction periods.

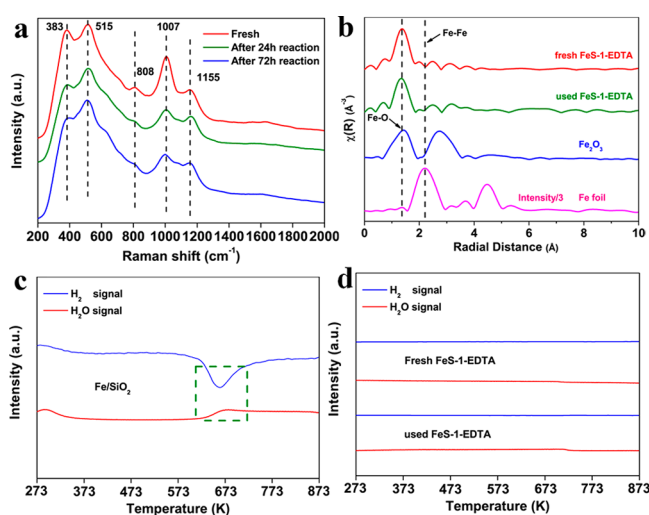


**Figure 3.** (a) UV resonance Raman ( $\lambda_{\text{ex}} = 325$  nm) and (b) EXAFS spectra of FeS-1-EDTA before and after catalysis in EDH. (c, d) H<sub>2</sub>-TPR profiles of various samples. Intensities of the longitudinal axis in c and d have the same proportion.

Besides the characteristic bands of the MFI zeolite structure at 383 and 808 cm<sup>-1</sup>, the catalysts are dominated by the 515, 1007, and 1155 cm<sup>-1</sup> bands, assigned to the framework tetrahedral iron species.<sup>38–40</sup> The Raman bands at 515 and 1155 cm<sup>-1</sup>, which are assigned to the symmetric and asymmetric stretching vibrations of the framework Fe<sup>δ+</sup>–O–Si species, are unchanged before and after catalysis, indicating the stable Fe<sup>δ+</sup>–O–Si linkage and isolated Fe sites during catalysis. The Raman band at 1007 cm<sup>-1</sup> is weakened on the used catalysts, which might be explained by formation of distorted tetrahedra units during the reaction (Figure S28). The extra framework Fe is always negligible even in the used catalyst, supporting the isolated Fe with Fe<sup>δ+</sup>–O–Si linkage on the catalysts. The local Fe coordination was studied by extended X-ray absorption fine structure (EXAFS) of the Fe K-edge. As shown in Figure 3b, the FeS-1-EDTA shows very

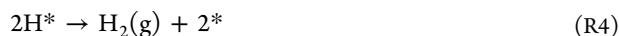
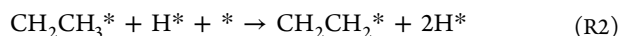
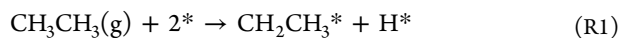
similar spectra with a strong signal of the first shell at 1.4 Å (without phase shift correction), assigned to Fe–O coordination. Notably, the signals of the Fe–Fe shells in metallic Fe or Fe<sub>2</sub>O<sub>3</sub> are undetectable due to the isolated Fe<sup>δ+</sup> sites on FeS-1-EDTA.<sup>41</sup> Interestingly, the sole Fe–O signal in EXAFS is still observed after 72 h reaction, suggesting that the isolated Fe<sup>δ+</sup> site is pretty stable. In addition, the ferric carbide (FeC<sub>x</sub>) species, which are easily formed on the Fe catalysts,<sup>36</sup> are not detected on the used FeS-1-EDTA (Figure 3b, C 1s XPS in Figure S29), suggesting that the carbonization is inhibited. In contrast, the FeS-1 catalyst has detectable extra-framework FeO<sub>x</sub> species in the UV–vis and Raman spectra (Figure S30). These species can lead to a reduction of the activity and coke formation that has been well studied previously.<sup>36</sup> The difference between FeS-1 and FeS-1-EDTA should be reasonably assigned to the EDTA in the synthesis gel (Figure S31), which stabilizes the isolated Fe sites to avoid formation of Fe(OH)<sub>3</sub> precipitate because of the stronger coordination of EDTA than that of OH<sup>-</sup> to the Fe<sup>3+</sup> sites. This feature could avoid the Fe precursor oligomerization in the zeolite crystallization system with strong alkalinity.

The sodium species was detected in FeS-1-EDTA, which cannot be avoided because EDTA–Na was used in the synthesis gel. Notably, such sodium species is insensitive to catalysis because an unchanged performance was still obtained on the catalyst with partial removal of sodium (Figure S32). In addition, the acidity, which is well known to occur in side reactions,<sup>23,41</sup> is extremely weak on the FeS-1-EDTA catalyst (Figure S33), which causes the performances to outperform the conventional aluminosilicate zeolite catalyst (e.g., Fe/ZSM-5-ex).

The antireduction ability of FeS-1-EDTA was evaluated by temperature-programmed reduction (H<sub>2</sub>-TPR) tests with a mass detector to collect the signals of H<sub>2</sub> (*m/z* at 2) and H<sub>2</sub>O (*m/z* at 18). As shown in Figure 3c, the signals of H<sub>2</sub> consumption and H<sub>2</sub>O formation appeared at 613–723 K on the Fe/SiO<sub>2</sub> samples, suggesting reduction of the FeO<sub>x</sub> species. Interestingly, the signals are completely undetectable on the as-synthesized and used FeS-1-EDTA catalysts even up to 873 K (Figure 3d), confirming the unreduced Fe<sup>δ+</sup> species. This phenomenon is reasonably attributed to modulation of the zeolite framework, where the SiO<sub>4</sub>–O–Fe<sup>δ+</sup> linkage stabilizes the isolated Fe<sup>δ+</sup> sites under harsh reaction conditions. Such feature should benefit ethene desorption rather than coke formation, leading to coke resistance. In contrast, the conventional supported ferric catalysts have reducible FeO<sub>x</sub> because of the lack of strong interaction with the silica, which forms a ferric carbide species that is well known as a highly active catalyst for deep dehydrogenation of ethene to coke (Figures S34 and S35).

**Mechanism Investigation.** Density functional theory (DFT) calculations were performed to understand the EDH mechanism on the FeS-1-EDTA (Fe–S-1 model with isolated Fe embedded in S-1 zeolite, see more details in SI), and various reference models included the transition metals (Pt, Pd, Fe), PtSn alloys, Ni–S-1, and Cu–S-1. The adsorption free energies of relevant intermediates over all studied catalysts were calculated and are listed in Tables S3 and S4. We first compared the reactivity of the terrace (111 and 110 for Fe) and step (211) facets of the transition metals. The terrace facets with better ethene selectivity are used to analyze the mechanism on metals and alloys (Figure S36). In addition, the tetrahedral iron and oxygen (Fe<sup>δ+</sup>–O<sup>(2-ξ)-</sup>) sites are more

unsaturated and reactive for ethane dehydrogenation compared to the structures of one or two H atoms binding with framework O (Figure S37). Hence, the site  $\text{Fe}^{\delta+}-\text{O}^{(2-\xi)-}$  is proposed to start the EDH reaction (Figure S38), and this process follows the reaction pathway



As the adsorption free energies of ethene,  $G_{\text{ad}}(\text{CH}_2\text{CH}_2^*)$ , over Fe, Pd, Pt, and PtSn alloy are tightly correlated with the other carbonaceous intermediates, the  $G_{\text{ad}}(\text{CH}_2\text{CH}_2^*)$  was chosen as the first descriptor to evaluate the trend of EDH activity. Note that there are two ethene adsorption structures for Metal-S-1 models via nonbonding weak  $\text{C}\cdots\text{H}$  interaction ( $\text{CH}_2\text{CH}_2^*\text{-a}$ ) or  $\text{C}-\text{O}$  bonding ( $\text{CH}_2\text{CH}_2^*\text{-b}$ ); the adsorption structures are shown in Figure S38. In addition, the adsorption free energies of hydrogen,  $G_{\text{ad}}(\text{H}^*)$ , are significantly different over the Metal-S-1 catalysts, which was chosen as the second descriptor. In general, the metal surfaces have much stronger  $G_{\text{ad}}(\text{CH}_2\text{CH}_2^*)$  than  $G_{\text{ad}}(\text{H}^*)$ , which could explain the favorable coke formation on the metallic catalysts. Interestingly, the zeolite S-1-modulated isolated sites (e.g., Fe) exhibit opposite character, showing stronger adsorption to  $\text{H}^*$  than to  $\text{CH}_2\text{CH}_2^*$ .

Figure 4 shows reaction free energies and two-dimensional phase diagrams (RPDs) for the EDH process (adsorption structures of intermediates on metals and alloy are shown in Figure S39). Overall, the intrinsic activity (conversion) of ethane over Pt, Pd, and PtSn is limited by the first step of ethane dehydrogenation (R1), while Fe(110) is the excep-

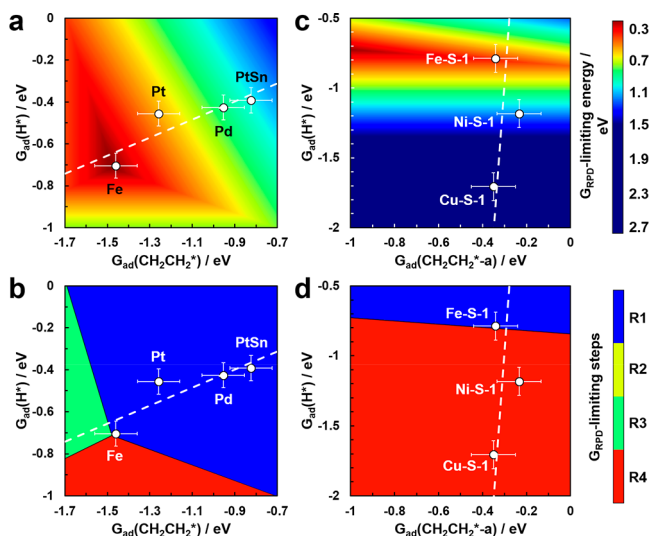


**Figure 4.** Two-dimensional reaction phase diagrams (RPDs) for the EDH reaction with the two descriptors  $G_{\text{ad}}(\text{H}^*)$  and  $G_{\text{ad}}(\text{CH}_2\text{CH}_2^*)$ , which is the ethene interacting with adsorbed hydrogen on the metal sites of Metal-S-1 models, illustrated as  $G_{\text{ad}}(\text{CH}_2\text{CH}_2^*\text{-a})$ .  $G_{\text{RPD}}$ -limiting energies are shown with reference to the color bar on the right over (a) transition metal surfaces and (c) isolated metal sites of Metal-S-1 catalysts.  $G_{\text{RPD}}$ -limiting steps for the EDH reaction over (b) transition metal surfaces and (d) isolated metal sites of Metal-S-1 catalysts (blue, R1; yellow, R2; green, R3; red, R4).

tional case, located at the border over R1, R3, and R4 (Figure 4b). In principle, Fe(110) should have great intrinsic activity (conversion) from a thermodynamic point of view. However, the observed deactivation of Fe catalysts should be a kinetic issue (see more explanation in the next section). On the contrary, hydrogen production and desorption (R4) is the key issue for the Metal-S-1 catalysts. According to Figure 4c, the Fe-S-1 is more active than Ni-S-1 and Cu-S-1 in the EDH reaction, as the relatively weak  $\text{H}^*$  adsorption on Fe-S-1 leads to facile  $\text{H}_2$  desorption. As shown in Figure 4d, the  $G_{\text{RPD}}$ -limiting step on Ni-S-1 and Cu-S-1 is hydrogen desorption (R4), while the most active Fe-S-1 is right located at the sweet intersection between ethane dehydrogenation (R1) and  $\text{H}_2$  desorption (R4).

For the kinetic issue over transition metal catalysts, it was found that the rate of ethane dehydrogenation (R1) determines the intrinsic activity (Figure S40a). Moreover, the rate of ethene desorption is inversely correlated with their strength of adsorption, as shown in Figure 5a. This indicates

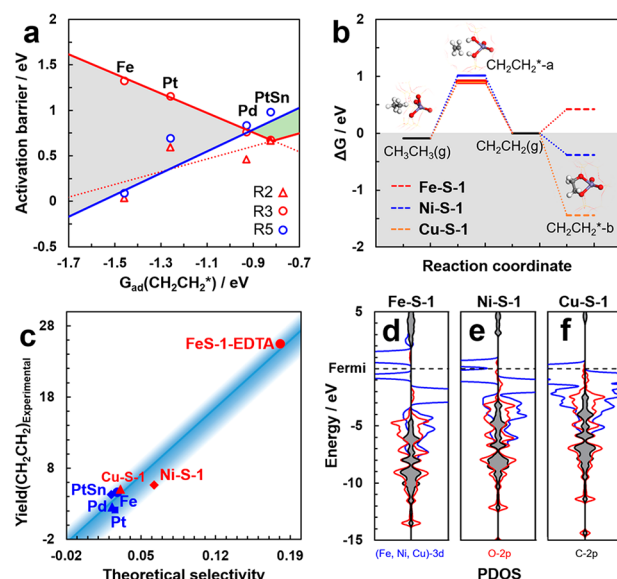


**Figure 5.** (a) Calculated activation barriers of  $\text{CH}_2\text{CH}_2^*$  desorption (R3) and  $\text{CH}_2\text{CH}_3^*$  dissociation (R2 and R5:  $\text{CH}_2\text{CH}_3^* + \text{H}^* + ^* \rightarrow \text{CH}_2\text{CH}_2^* + 2\text{H}^*$ ), where R2 and R3 are important for selective ethene production, while R5 is assumed to be the main route for coke formation (see more details in SI). (b) Reaction free energies and paths for ethane dehydrogenation to ethene, and first step of coke formation ( $\text{CH}_2\text{CH}_2^*\text{-b}$ ). (c) Comparison of the theoretically calculated activity over all studied catalysts with experimental yield of  $\text{CH}_2\text{CH}_2$ . (d–f) Projected density of states for the  $\text{CH}_2\text{CH}_2^*\text{-b}$  structures over Metal-S-1 models with (d) Fe, (e) Ni, and (f) Cu sites. The 3d band states of Fe, Ni, and Cu sites on the S-1 zeolite and 2p-O and 2p-C of adsorbed  $\text{CH}_2\text{CH}_2^*$  are shown in blue, red, and gray, respectively.

that the most reactive Fe catalyst will be poisoned and deactivated with too high coverage of  $\text{C}_x\text{H}_y$ , resulting in coking and low ethene productivity. In order to estimate the influence of coke on activity, a coke-resistant coefficient  $\theta$  was introduced in this work, allowing us to develop the microkinetic model for ethene yield estimation (see more details in SI). Different from metals, the intrinsic activity of Metals-S-1 is correlated with the activation barriers of hydrogen desorption (R4), as the ethane dehydrogenation step has lower barriers than R4 (Figure S40b). In addition, the

key factor of coke resistance is the strength of ethene adsorption landing on oxygen ( $\text{CH}_2\text{CH}_2^*\text{-b}$ ), as shown in Figure 5b. For zeolite-modulated Fe sites, as the strong electronic interaction between Fe and O elements, the bonding states are far below the Fermi level, resulting in limited electronic states available for direct interaction with  $\text{CH}_2\text{CH}_2^*$ . Hence, the ethene adsorption [ $G_{\text{ad}}(\text{CH}_2\text{CH}_2^*\text{-b})$ ] is not favorable (+0.42 eV), which should benefit desorption of the ethene product before coking in a practical reaction. For the Ni and Cu sites on zeolite, the electronic states of oxygen are shifted higher, closer to the Fermi level, which leads to stronger ethene adsorption free energies (−0.38 eV for Ni and −1.44 eV for Cu). In short, the Fe in the zeolite exhibits an optimal character for ethane conversion, hydrogen desorption, and selective ethene desorption. Although it has been known that the Ni and Cu catalysts are not active for the dehydrogenation, in the present study we provide a mechanistic understanding for this phenomenon.

In order to compare the catalytic performance for all of the transition metal and Metal-S-1 catalysts, both the intrinsic activity (activation energies) and the coke-resistant coefficient are used to predict the ethene yield. The results are shown in Figure 5c. From a selectivity point of view, the PtSn alloy should exhibit an optimal balance over all transition metal catalysts (Figure 5a), while it is still below the Fe–S-1 (FeS-1-EDTA) catalyst (Figure 5c).

We further performed a kinetic study to identify the theoretical hypothesis. Figure S41 shows kinetic data of the FeS-1-EDTA catalyst in the EDH, giving an apparent activation energy of 117.8 kJ mol<sup>−1</sup>, which is lower than 129.8 kJ mol<sup>−1</sup> on the Fe/SiO<sub>2</sub> catalyst, suggesting that the reaction on the FeS-1-EDTA is easier. The Fe/SiO<sub>2</sub> shows the reaction order to ethane at 1.1. In contrast, the FeS-1-EDTA gives the reaction order to ethane at 0.6, much lower than that of Fe/SiO<sub>2</sub>, confirming the favorable ethane adsorption on the FeS-1-EDTA catalyst because of the negative correlation between the adsorption entropy and the reaction order. This phenomenon is in good agreement with the DFT results, where the difficult to desorb intermediates suppress the ethane adsorption on the FeO<sub>x</sub> catalysts. Figure S42a shows the data plots characterizing the reaction order to hydrogen, showing −1.89 on Fe/SiO<sub>2</sub> and −0.66 on FeS-1-EDTA. A lower reaction order suggests that ethane conversion is less affected by hydrogen in EDH on the FeS-1-EDTA, which might be related to its weakened adsorption to hydrogen as revealed by the theoretical simulation and temperature-programmed desorption of H<sub>2</sub> (Figure S42b).

## CONCLUSION

In summary, we reported an efficient and nonprecious catalyst for dehydrogenation of ethane. The catalyst, named FeS-1-EDTA, exhibits high activity, selectivity, and superior durability for the EDH to ethene. Detailed characterization demonstrates the siliceous zeolite framework modulates and stabilizes the isolated ferric sites to avoid the ferric species reduction that causes coke formation and deactivation. In addition, the Fe–zeolite structure balances ethane dehydrogenation as well as ethene and hydrogen desorption, which eventually accelerate ethane conversion and avoid coke formation, rationalized well by our density functional calculations and microkinetic modeling. The advantages of isolated Fe embedded in zeolite micropores are quite helpful for exploration of on-purpose ethene technologies.

## ASSOCIATED CONTENT

### Supporting Information

The Supporting Information is available free of charge at <https://pubs.acs.org/doi/10.1021/jacs.0c07792>.

XRD, N<sub>2</sub> sorption, STEM images, SEM images, XPS, Raman, TG, and more catalysis and DFT data (PDF)

## AUTHOR INFORMATION

### Corresponding Authors

**Liang Wang** – Key Lab of Biomass Chemical Engineering of Ministry of Education, College of Chemical and Biological Engineering, Zhejiang University, Hangzhou 310027, China; [orcid.org/0000-0002-5826-1866](https://orcid.org/0000-0002-5826-1866); Email: [liangwang@zju.edu.cn](mailto:liangwang@zju.edu.cn)

**Jianping Xiao** – State Key Laboratory of Catalysis, Dalian Institute of Chemical Physics, Chinese Academy of Sciences, Dalian 116023, China; [orcid.org/0000-0003-1779-6140](https://orcid.org/0000-0003-1779-6140); Email: [xiao@dicp.ac.cn](mailto:xiao@dicp.ac.cn)

**Feng-Shou Xiao** – Key Lab of Biomass Chemical Engineering of Ministry of Education, College of Chemical and Biological Engineering and Key Lab of Applied Chemistry of Zhejiang Province, Department of Chemistry, Zhejiang University, Hangzhou 310027, China; [orcid.org/0000-0001-9744-3067](https://orcid.org/0000-0001-9744-3067); Email: [fsxiao@zju.edu.cn](mailto:fsxiao@zju.edu.cn)

### Authors

**Zhiyuan Yang** – Key Lab of Biomass Chemical Engineering of Ministry of Education, College of Chemical and Biological Engineering and Key Lab of Applied Chemistry of Zhejiang Province, Department of Chemistry, Zhejiang University, Hangzhou 310027, China

**Huan Li** – State Key Laboratory of Catalysis, Dalian Institute of Chemical Physics, Chinese Academy of Sciences, Dalian 116023, China

**Hang Zhou** – Key Lab of Biomass Chemical Engineering of Ministry of Education, College of Chemical and Biological Engineering, Zhejiang University, Hangzhou 310027, China

**Lingxiang Wang** – Key Lab of Applied Chemistry of Zhejiang Province, Department of Chemistry, Zhejiang University, Hangzhou 310028, China; [orcid.org/0000-0003-0665-8594](https://orcid.org/0000-0003-0665-8594)

**Qiuyan Zhu** – Key Lab of Applied Chemistry of Zhejiang Province, Department of Chemistry, Zhejiang University, Hangzhou 310028, China

**Xiangju Meng** – Key Lab of Applied Chemistry of Zhejiang Province, Department of Chemistry, Zhejiang University, Hangzhou 310028, China; [orcid.org/0000-0001-8740-2755](https://orcid.org/0000-0001-8740-2755)

**Junxiang Chen** – Division of China, TILON Group Technology Limited, Shanghai 200090, China

Complete contact information is available at: <https://pubs.acs.org/doi/10.1021/jacs.0c07792>

### Author Contributions

This manuscript was written through contribution of all authors.

### Author Contributions

<sup>||</sup>Z.Y., H.L., and H.Z.: These authors contributed equally.

### Notes

The authors declare no competing financial interest.



## ■ ACKNOWLEDGMENTS

This work was supported by the National Key Research and Development Program of China (2018YFB0604801), National Natural Science Foundation of China (91634201, 21822203, 91945302, 21802124, and 91845103), Natural Science Foundation of Zhejiang Province (LR18B030002), fund from Central University (2019XZZX004-02), Strategic Priority Research Program of the Chinese Academy of Sciences (No. XDB36030200), and Liaoning Revitalization Talents program (No. XLYC1907099). We thank Fang Chen for help with TEM characterization. We acknowledge beamtime at Shanghai Synchrotron Radiation Facility (SSRF, beamline BL14W1).

## ■ REFERENCES

- (1) Gomez, E.; Yan, B. H.; Kattel, S.; Chen, J. G. Carbon dioxide reduction in tandem with light-alkane dehydrogenation. *Nat. Rev. Chem.* **2019**, *3*, 638–649.
- (2) Shi, L.; Deng, G.-M.; Li, W.-C.; Miao, S.; Wang, Q.-N.; Zhang, W.-P.; Lu, A.-H.  $\text{Al}_2\text{O}_3$  nanosheets rich in pentacoordinate  $\text{Al}^{3+}$  ions stabilize Pt-Sn clusters for propane dehydrogenation. *Angew. Chem., Int. Ed.* **2015**, *54*, 13994–13998.
- (3) Bao, J.; Yang, G.; Yoneyama, Y.; Tsubaki, N. Significant advances in  $\text{C}_1$  catalysis: Highly efficient catalysts and catalytic reactions. *ACS Catal.* **2019**, *9*, 3026–3053.
- (4) Sattler, J. J. H. B.; Ruiz-Martinez, J.; Santillan-Jimenez, E.; Weckhuysen, B. M. Catalytic dehydrogenation of light alkanes on metals and metal oxides. *Chem. Rev.* **2014**, *114*, 10613–10653.
- (5) Saththawong, R.; Koizumi, N.; Song, C. S.; Prasassarakich, P. Light olefin synthesis from  $\text{CO}_2$  hydrogenation over K-promoted Fe-Co bimetallic catalysts. *Catal. Today* **2015**, *251*, 34–40.
- (6) Tian, P.; Wei, Y.; Ye, M.; Liu, Z. Methanol to olefins (MTO): From fundamentals to commercialization. *ACS Catal.* **2015**, *5*, 1922–1938.
- (7) Gao, Y.; Wang, X.; Liu, J.; Huang, C.; Zhao, K.; Zhao, Z.; Wang, X.; Li, F. A molten carbonate shell modified perovskite redox catalyst for anaerobic oxidative dehydrogenation of ethane. *Sci. Adv.* **2020**, *6*, eaaz9339.
- (8) Calviere, V. N.; Crestani, M. G.; Pinter, B.; Pink, M.; Chen, C.-H.; Baik, M.-H.; Mendiola, D. J. Room temperature dehydrogenation of ethane to ethylene. *J. Am. Chem. Soc.* **2011**, *133*, 10700–10703.
- (9) Porosoff, M. D.; Myint, M. N. Z.; Kattel, S.; Xie, Z. H.; Gomez, E.; Liu, P.; Chen, J. G. Identifying different types of catalysts for  $\text{CO}_2$  reduction by ethane through dry reforming and oxidative dehydrogenation. *Angew. Chem., Int. Ed.* **2015**, *54*, 15501–15505.
- (10) Melzer, D.; Xu, P. H.; Hartmann, D.; Zhu, Y. Y.; Browning, N. D.; Sanchez-Sanchez, M.; Lercher, J. A. Atomic-scale determination of active facets on the  $\text{MoVTaNb}$  oxide M1 phase and their intrinsic catalytic activity for ethane oxidative dehydrogenation. *Angew. Chem., Int. Ed.* **2016**, *55*, 8873–8877.
- (11) Grant, J. T.; Carrero, C. A.; Goeltl, F.; Venegas, J.; Mueller, P.; Burt, S. P.; Specht, S. E.; McDermott, W. P.; Chierigato, A.; Hermans, I. Selective oxidative dehydrogenation of propane to propene using boron nitride catalysts. *Science* **2016**, *354*, 1570–1573.
- (12) Zhang, X. Y.; You, R.; Wei, Z. Y.; Jiang, X.; Yang, J. Z.; Pan, Y.; Wu, P. W.; Jia, Q. D.; Bao, Z. H.; Bai, L.; Jin, M. Z.; Sumpter, B.; Fung, V.; Huang, W. X.; Wu, Z. L. Radical chemistry and reaction mechanisms of propane oxidative dehydrogenation over hexagonal boron nitride catalysts. *Angew. Chem., Int. Ed.* **2020**, *59*, 8042–8046.
- (13) Vajda, S.; Pellin, M. J.; Greeley, J. P.; Marshall, C. L.; Curtiss, L. A.; Ballentine, G. A.; Elam, J. W.; Catillon-Mucherie, S.; Redfern, P. C.; Mehmood, F.; Zapol, P. Subnanometer platinum clusters as highly active and selective catalysts for the oxidative dehydrogenation of propane. *Nat. Mater.* **2009**, *8*, 213–216.
- (14) Chen, S.; Zeng, L.; Mu, R. T.; Xiong, C. Y.; Zhao, Z. J.; Zhao, C. J.; Pei, C. L.; Peng, L. M.; Luo, J.; Fan, L. S.; Gong, J. L. Modulating lattice oxygen in dual-functional Mo-V-O mixed oxides for chemical looping oxidative dehydrogenation active and selective catalysts for the oxidative dehydrogenation of propane. *J. Am. Chem. Soc.* **2019**, *141*, 18653–18657.
- (15) Lu, J.; Fu, B.; Kung, M. C.; Xiao, G.; Elam, J. W.; Kung, H. H.; Stair, P. C. Coking- and sintering-resistant palladium catalysts achieved through atomic layer deposition. *Science* **2012**, *335*, 1205–1208.
- (16) Zhang, T.; Sole-Daura, A.; Hostachy, S.; Blanchard, S.; Paris, C.; Li, Y.; Carbo, J. J.; Poblet, J. M.; Proust, A.; Guillemot, G. Modeling the oxygen vacancy at a molecular vanadium(III) silica-supported catalyst. *J. Am. Chem. Soc.* **2018**, *140*, 14903–14914.
- (17) Bian, Y. X.; Kim, M.; Li, T.; Asthagiri, A.; Weaver, J. F. Facile dehydrogenation of ethane on the  $\text{IrO}_2(110)$  surface. *J. Am. Chem. Soc.* **2018**, *140*, 2665–2672.
- (18) Li, Z. Y.; Peters, A. W.; Platero-Prats, A. E.; Liu, J.; Kung, C.-W.; Noh, H.; DeStefano, M. R.; Schweitzer, N. M.; Chapman, K. W.; Hupp, J. T.; Farha, O. K. Fine-tuning the activity of metal-organic framework-supported cobalt catalysts for the oxidative dehydrogenation of propane. *J. Am. Chem. Soc.* **2017**, *139*, 15251–15258.
- (19) Cheng, M.-J.; Goddard, W. A., III In silico design of highly selective Mo-V-Te-Nb-O mixed metal oxide catalysts for ammoxidation and oxidative dehydrogenation of propane and ethane. *J. Am. Chem. Soc.* **2015**, *137*, 13224–13227.
- (20) Sun, Q. M.; Wang, N.; Fan, Q. Y.; Zeng, L.; Mayoral, A.; Miao, S.; Yang, R.; Jiang, Z.; Zhou, W.; Zhang, J. C.; Zhang, T. J.; Xu, J.; Zhang, P.; Cheng, J.; Yang, D. C.; Jia, R.; Li, L.; Zhang, Q. H.; Wang, Y.; Terasaki, O.; Yu, J. H. Subnanometer bimetallic platinum–zinc clusters in zeolites for propane dehydrogenation. *Angew. Chem., Int. Ed.* **2020**, *59*.
- (21) Taccardi, N.; Grabau, M.; Debuschewitz, J.; Distaso, M.; Brandl, M.; Hock, R.; Maier, F.; Papp, C.; Erhard, J.; Neiss, C.; Peukert, W.; Görling, A.; Steinrück, H.-P.; Wasserscheid, P. Gallium-rich Pd–Ga phases as supported liquid metal catalysts. *Nat. Chem.* **2017**, *9*, 862–867.
- (22) Maeno, Z.; Yasumura, S.; Wu, X. P.; Huang, M. W.; Liu, C.; Toyao, T.; Shimizu, K. I. Isolated Indium-hydrides in CHA Zeolites: Speciation and catalysis for non-oxidative dehydrogenation of ethane. *J. Am. Chem. Soc.* **2020**, *142*, 4820–4832.
- (23) Wang, L. C.; Zhang, Y. Y.; Xu, J. Y.; Diao, W. J.; Karakalos, S.; Liu, B.; Song, X. Y.; Wu, W.; He, T.; Ding, D. Non-oxidative dehydrogenation of ethane to ethylene over ZSM-5 zeolite supported iron catalysts. *Appl. Catal., B* **2019**, *256*, 117816.
- (24) Phadke, N. M.; Mansoor, E.; Bondil, M.; Head-Gordon, M.; Bell, A. T. Mechanism and kinetics of propane dehydrogenation and cracking over Ga/H-MFI prepared via vapor-phase exchange of H-MFI with  $\text{GaCl}_3$ . *J. Am. Chem. Soc.* **2019**, *141*, 1614–1627.
- (25) Searles, K.; Chan, K. W.; Mendes Burak, J. A.; Zemlyanov, D.; Safonova, O.; Coperet, C. Highly productive propane dehydrogenation catalyst using silica-supported Ga–Pt nanoparticles generated from single-sites. *J. Am. Chem. Soc.* **2018**, *140*, 11674–11679.
- (26) Xiong, H. F.; Lin, S.; Goetze, J.; Pletcher, P.; Guo, H.; Kovarik, L.; Artyushkova, K.; Weckhuysen, B. M.; Datye, A. K. Thermally stable and regenerable platinum–tin clusters for propane dehydrogenation prepared by atom trapping on ceria. *Angew. Chem., Int. Ed.* **2017**, *56*, 8986–8991.
- (27) Nakaya, Y.; Hirayama, J.; Yamazoe, S.; Shimizu, K.-i.; Furukawa, S. Single-atom Pt in intermetallics as an ultrastable and selective catalyst for propane dehydrogenation. *Nat. Commun.* **2020**, *11*, 2838.
- (28) Sattler, J. J. H. B.; Gonzalez-Jimenez, I. D.; Luo, L.; Stears, B. A.; Malek, A.; Barton, D. G.; Kilos, B. A.; Kaminsky, M. P.; Verhoeven, T. W. G. M.; Koers, E. J.; Baldus, M.; Weckhuysen, B. M. Platinum-promoted Ga/ $\text{Al}_2\text{O}_3$  as highly active, selective, and stable catalyst for the dehydrogenation of propane. *Angew. Chem., Int. Ed.* **2014**, *53*, 9251–9256.
- (29) Liu, L.; Lopez-Haro, M.; Lopes, C. W.; Li, C.; Concepcion, P.; Simonelli, L.; Calvino, J. J.; Corma, A. Regioselective generation and reactivity control of subnanometric platinum clusters in zeolites for high-temperature catalysis. *Nat. Mater.* **2019**, *18*, 866–873.

- (30) Ji, Z. H.; Lv, H. F.; Pan, X. L.; Bao, X. H. Enhanced ethylene selectivity and stability of Mo/ZSM-5 upon modification with phosphorus in ethane dehydrogenation. *J. Catal.* **2018**, *361*, 94–104.
- (31) Siahvashi, A.; Chesterfield, D.; Adesina, A. A. Nonoxidative and oxidative propane dehydrogenation over bimetallic Mo–Ni/Al<sub>2</sub>O<sub>3</sub> catalyst. *Ind. Eng. Chem. Res.* **2013**, *52*, 4017–4026.
- (32) Tan, S.; Kim, S. J.; Moore, J. S.; Liu, Y. J.; Dixit, R. S.; Pendergast, J. G.; Sholl, D. S.; Nair, S.; Jones, C. W. Propane dehydrogenation over In<sub>2</sub>O<sub>3</sub>–Ga<sub>2</sub>O<sub>3</sub>–Al<sub>2</sub>O<sub>3</sub> mixed oxides. *ChemCatChem* **2016**, *8*, 214–221.
- (33) Almutairi, S. M. T.; Mezari, B.; Magusin, P. C. M. M.; Pidko, E. A.; Hensen, E. J. M. Structure and reactivity of Zn-modified ZSM-5 zeolites: The importance of clustered cationic Zn complexes. *ACS Catal.* **2012**, *2*, 71–83.
- (34) Sun, G. D.; Zhao, Z.-J.; Mu, R.; Zha, S.; Li, L.; Chen, S.; Zang, K.; Luo, J.; Li, Z.; Purdy, S.; Kropf, A. J.; Miller, J. T.; Zeng, L.; Gong, J. L. Breaking the scaling relationship via thermally stable Pt/Cu single atom alloys for catalytic dehydrogenation. *Nat. Commun.* **2018**, *9*, 4454.
- (35) Zhao, Z.; Chiu, C.-C.; Gong, J. L. Molecular understandings on the activation of light hydrocarbons over heterogeneous catalysts. *Chem. Sci.* **2015**, *6*, 4403–4425.
- (36) Hu, B.; Schweitzer, N. M.; Zhang, G. H.; Kraft, S. J.; Childers, D. J.; Lanci, M. P.; Miller, J. T.; Hock, A. S. Isolated Fe<sup>II</sup> on silica as a selective propane dehydrogenation catalyst. *ACS Catal.* **2015**, *5*, 3494–3503.
- (37) Liu, X.; Lang, W. Z.; Long, L. L.; Hu, C. L.; Chu, L. F.; Guo, Y. J. Improved catalytic performance in propane dehydrogenation of PtSn/ $\gamma$ -Al<sub>2</sub>O<sub>3</sub> catalysts by doping indium. *Chem. Eng. J.* **2014**, *247*, 183–192.
- (38) Ju, X. H.; Tian, F. P.; Wang, Y. L.; Fan, F. T.; Feng, Z. C.; Li, C. A novel synthetic strategy of Fe-ZSM-35 with pure framework Fe species and its formation mechanism. *Inorg. Chem. Front.* **2018**, *5*, 2031.
- (39) Wang, J. Y.; Li, G. N.; Ju, X. H.; Xia, H. A.; Fan, F. T.; Wang, J. H.; Feng, Z. C.; Li, C. Identification of Fe<sub>2</sub>(l-O) and Fe<sub>2</sub>(l-O)<sub>2</sub> sites in Fe/ZSM-35 by in situ resonance Raman spectroscopy. *J. Catal.* **2013**, *301*, 77–82.
- (40) Wang, J. Y.; Xia, H. A.; Ju, X. H.; Feng, Z. C.; Fan, F. T.; Li, C. Influence of extra-framework Al on the structure of the active iron sites in Fe/ZSM-35. *J. Catal.* **2013**, *300*, 251–259.
- (41) Huggins, F. E.; Shen, W. Q.; Cprek, N.; Shah, N.; Marinkovic, N. S.; Huffman, G. P. In situ X-ray absorption near-edge structure (XANES) spectroscopic investigation of the pre-reduction of iron-based catalysts for non-oxidative alkane dehydrogenation. *Energy Fuels* **2008**, *22*, 3620–3625.